



Topological effects of 3D-printed copolymer interlayers on toughening and in situ self-healing in laminated fiber-composites

Jack S. Turicek^a, Alexander D. Snyder^a, Kalyana B. Nakshatrala^b, Jason F. Patrick^{a,c,*}

^a Department of Mechanical and Aerospace Engineering, North Carolina State University, Raleigh, 27695, NC, USA

^b Department of Civil and Environmental Engineering, University of Houston, Houston, 77204, TX, USA

^c Department of Civil, Construction, and Environmental Engineering, North Carolina State University, Raleigh, 27695, NC, USA

ARTICLE INFO

Keywords:

- A. Self-healing
- B. Damage tolerance
- C. Interlaminar delamination
- D. Thermal remending
- E. Multifunctional

ABSTRACT

Interlaminar delamination in fiber-reinforced composites limits structural capacity and service life. Delaminations, which occur subsurface and can lead to catastrophic failures, are hard to detect and repair. Contrasting traditional mitigation strategies (e.g., inspection, over-design), proactive toughening and responsive self-healing of damaged interfaces offer practical, cost-effective solutions. Our recently developed strategy to address interlaminar damage—3D-printed thermoplastic interlayers and structurally integrated heaters—has been shown to achieve composite toughening and *in situ* self-healing via thermal remending, abetting repeated repair and improved delamination resistance. Here, we leverage this latest thermal remending strategy to investigate the effects of 3D-printed pattern topology on damage resistance and self-healing response. The chief attributes are: (i) realizing up to 450% increase in mode-I fracture resistance, (ii) restoring up to 100% of the increased fracture resistance for ten consecutive healing cycles, and (iii) achieving *in situ* self-healing below the thermoset-matrix glass transition temperature, thereby preserving structural integrity during repair. The proposed damage mitigation strategy fosters structural reliability, reduces failure risk, and increases service lifetime—three essential attributes in meeting the multifaceted demands of modern composite infrastructure.

1. Introduction

Fiber-reinforced polymer (FRP) composites possess advantageous properties such as high specific strength/stiffness and corrosion resistance, to name a few. Such properties are why polymer-matrix composites have become a chief infrastructural material when dealing with demanding environments in aerospace, naval, civil, and energy applications. FRP composites derive their attributes from hierarchical material makeup, rendering them susceptible to complex damage modes, e.g., failure within constituent materials or adjoining interfaces. Interlaminar delamination (i.e., interfacial debonding of the polymer matrix from the fibrous reinforcement) remains a dominant damage mode in FRP composites [1]. Delaminations occur subsurface that require advanced detection and monitoring techniques, which have experienced mixed success [2,3]. Hence, repair of such interfacial damage currently requires intensive manual intervention and often replacement of the entire affected component [4,5]. Importantly, undetected or unaddressed interlaminar delaminations can lead to catastrophic failures. The conventional strategies to mitigate this risk are over-design and service lifetime restriction; however, these strategies are neither economical (e.g., cost and supply chain concerns) nor environmentally

friendly (e.g., recycling limitations). Thus, there is a crucial need to develop novel methodologies to broaden sustainability and unlock the unrealized potential of FRP composite materials for modern engineered structures.

Contemporary damage mitigation strategies focus on proactive *toughening* or responsive *self-healing*. Toughening brittle FRP composites increases resistance to delamination and has been achieved in many forms: modifying thermoset (e.g., epoxy) matrices via addition of a dispersed secondary phase (i.e., rubber or thermoplastic [6–9]), using thermoplastic matrices [10,11], or incorporating interlayers between reinforcement laminae [12–14]. In each case, the modification toughens the composite by either increasing the tortuosity of the crack path or absorbing energy through plastic deformation [15,16]. However, a primary drawback of these methods is a decrease in composite stiffness and thermal stability because of the widespread inclusion of a more compliant and meltable polymer into the structural composite [17]. Thus, the need to preserve FRP composite's bulk thermomechanical properties warrants a local deployment of toughening agents—only to sites that are prone to fracture.

* Corresponding author at: Department of Civil, Construction, and Environmental Engineering, North Carolina State University, Raleigh, 27695, NC, USA.
E-mail address: jfpatric@ncsu.edu (J.F. Patrick).

In contrast to toughening (a proactive measure), self-healing is a *responsive* measure for addressing delamination in composites [18]. The notable advantage of this alternative is the ability to self-repair fabrication defects or damage introduced during service. Consequently, self-healing is especially advantageous in extreme, dangerous, and inaccessible environments (e.g., outer space, offshore, in-flight) [19]. Self-healing is broadly classified into extrinsic and intrinsic approaches [20, 21]. *Extrinsic* self-healing relies on external healing agents typically sequestered within embedded microcapsules [22], hollow glass fibers [23], or vascular networks [24]. Microcapsule-based healing stores reactive liquids within spherical capsules dispersed throughout the host matrix, whereas hollow glass fibers contain healing chemistries inside cylindrical micro-tubes within or between textile reinforcement. In either case, the vessels rupture upon local fracture and release their payload into the proximal crack. Subsequent polymerization occurs via contact with a solid catalyst (for a one-part liquid agent) or diffusion plus mixing in the case of two-part healing chemistries. While autonomic (i.e., no human intervention required), such systems are limited to small damage volumes (μm -scale) and to a single healing event once the liquid agent is deployed [25]. For overcoming such hurdles (i.e., repair larger damage volumes and retain functionality over multiple damage–heal cycles), microvascular-based self-healing arose. This bioinspired strategy creates a network of microchannels within the host material that enables greater storage of healing agents and repeated delivery to the damage site via passive capillary action or active pumping [26–30]. However, vascular self-healing is often limited by *in situ* mixing requirements in the damage zone, thus relying on slower molecular diffusion for polymerization reactions to occur. Other vascular hindrances include flow restriction from healing agent accumulation and channel blockages resulting from cross-contamination. While the inclusion of capsules, hollow glass fibers, or vasculature have shown some ability to toughen polymer composites against delamination [28,31,32], the main advantage of these techniques is not their ability to resist fracture, but to functionally repair it.

Unlike extrinsic techniques, *intrinsic* self-healing materials possess the innate ability to self-repair [25]. Provided intimate contact of fractured interfaces is attained, self-healing is achieved via dynamic and reversible chemical bonds that are able to repeatedly reform after damage [33,34]. Intrinsic healing is more accessible in soft polymers (e.g., gels, rubbers) [35–38] with mechanical properties not suitable for structural applications. On the other hand, rigid structural materials (e.g., epoxies, vitrimers) [39] typically require an external energy source such as heat [40,41], light [42,43], or mechanical input [44] to enable bond reformation and thus initiate healing.

New hybrid extrinsic/intrinsic self-healing approaches continue to emerge that leverage the inclusion of a soft, intrinsically healable agent within a stiffer structural host material [45]. Such systems hold promise for both proactive damage resistance and responsive repair where the added toughening component not only resists delamination, but also serves as a healing agent to repeatedly repair damage when it occurs. One toughening/healing agent that has been extensively studied in FRP composites is poly(ethylene-co-methacrylic acid) (EMAA) [46–54]. Various morphologies of EMAA have been integrated into FRP composite laminates, including (i) particles dispersed throughout a thermoset matrix [49,51,53], (ii) fibers that are stitched or braided/woven within a fibrous preform [50,52,54], and (iii) meshes/films placed between reinforcing plies [46,48]. Laminated composite toughening and heat-initiated intrinsic healing of EMAA thermoplastic (i.e., thermal remending) are unique compared to other thermoplastic agents (e.g., polycaprolactone, PCL) [55] due to beneficial chemical reactions. During thermal remending, condensation reactions between methacrylic acid groups in the EMAA and tertiary amines in the epoxy matrix produce pressurizing water vapor that forces molten thermoplastic into confined damage volumes [51,56,57]. While effective for healing agent delivery, thermal remending at elevated temperatures must remain sufficiently

below the glass-transition temperature (T_g) of the thermoset epoxy matrix to retain structural integrity during repair. Moreover, to be industry transferable, thermal remending requires standalone heat generation (i.e., *in situ* healing) as opposed to popular *ex situ* recovery by placing composite components into an oven for repair [46,47,49,51–54]

Recently, resistive heater interlayers in glass- and carbon-fiber reinforced epoxy–matrix composites have been combined with 3D-printed EMAA to achieve sub- T_g *in situ* thermal remending of interlaminar delamination [58]. An unprecedented 100 heal cycles was achieved by EMAA failing in a cohesive manner (i.e., EMAA adhered to both fracture surfaces), and thus enabling repeated chain re-entanglement. Cohesive fracture relies on three critical attributes: (i) printing molten EMAA directly onto the fiber reinforcement, (ii) further “melt-bonding” prior to epoxy matrix infusion, and (iii) covalent/ionic bonding of the EMAA to the digcidyl ether of bisphenol A (DGEBA) epoxy matrix that strengthens the EMAA/DGEBA interface. However, the effects of the EMAA serpentine pattern orientation and thickness on toughening behavior and self-healing performance have not yet been explored. This work thoroughly investigates the interlaminar fracture behavior for a 3D-printed serpentine EMAA interlayer with different as-printed areal coverages, orientations, and thicknesses in glass fiber-reinforced polymer (GFRP) composite laminates. The mode-I critical strain energy release rate (G_{IC}) is calculated to characterize the overall interlaminar fracture energy, while resistance curves (R-curves) for each EMAA pattern are constructed to study the localized toughening behavior throughout delamination propagation. Repeated *in situ* thermal remending is achieved for different areal coverages and orientations at healing temperatures below the T_g of the host epoxy matrix. Quasistatic in-plane tension testing and dynamic mechanical analysis (DMA) of laminates with printed EMAA patterns are also conducted to assess thermo-mechanical integrity after augmentation. The comprehensive results from this study provide guidance for real-world translation of such hybrid self-healing and multifunctional FRP composites.

2. Materials and methods

2.1. 3D printing of EMAA via Fused Deposition Modeling (FDM)

EMAA filament with a diameter ≈ 2.5 mm was produced from as-purchased pellets of Nucrel™ 2940 (Dow Chemical, Inc.) using a single screw extruder (Filastruder, Inc.) with a 3 mm diameter circular die and 110 °C barrel temperature. Molten EMAA was collected on a rotating steel take-up cylinder (diameter = 165 mm) and cooled down to room temperature (RT, ≈ 23 °C) via forced convection from a proximal fan.

Molten EMAA filament was then patterned onto 8-Harness (8H) satin woven E-glass reinforcement (Style 7781, Hexcel, Inc.) using a TAZ Pro FDM printer (Lulzbot, Inc.) with a 500 μm diameter nozzle heated to 190 °C and a bed temperature of 65 °C. The printing process is depicted in Fig. 1a, where the computer-controlled print head/nozzle deposits molten EMAA directly onto the woven reinforcement, which ensures adhesion between the EMAA and the textile substrate. Different patterns were explored in this study by varying thickness (t), width (w), and spacing (s). Continuous serpentine patterns, shown in Fig. 1b, were orientated with primary traces either parallel (i.e., longitudinal, L) or perpendicular (i.e., transverse, T) to the crack propagation direction (0°). The optical microscope images provided in Fig. 1c show precise pattern spacing and cross-sectional control for EMAA printing. A complementary scanning electron micrograph, shown in Fig. 1d, indicates the underlying reinforcement architecture remains undisturbed by the FDM process (i.e., printing does not induce tow misalignment).

As-printed areal coverage, orientation, and thickness define EMAA patterns. Areal coverage—the printed area of EMAA divided by the encompassing area of the underlying reinforcement—was investigated for 12, 24, and 36%. As-printed EMAA thickness was varied from 150, 300, and 450 μm .

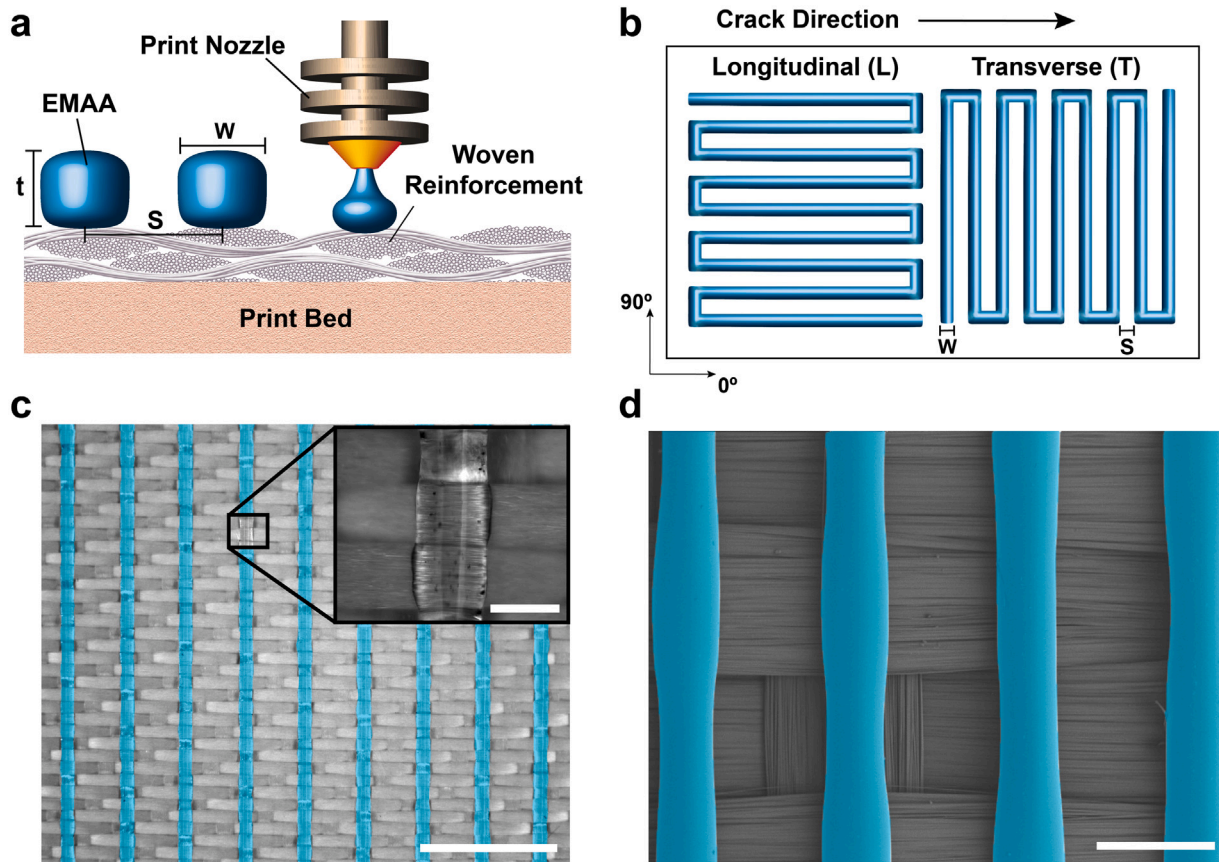


Fig. 1. Patterning EMAA via 3D-printing. (a) A depiction of the fused deposition modeling (FDM) process in which the computer-controlled print head/nozzle continuously extrudes molten EMAA thermoplastic of desired thickness (t), width (w), and spacing (s) directly on woven reinforcement. (b) Longitudinal (L) and transverse (T) serpentine pattern orientations in reference to the crack propagation direction (0°). (c) Optical microscope images of printed EMAA (blue overlay) on 8H satin E-glass fabric (main scale bar = 5 mm, inset scale bar = 0.5 mm). (d) Scanning electron micrograph of as-printed EMAA pattern on woven reinforcement (scale bar = 1 mm).

2.2. Preform construction and melt consolidation

Following 3D-printing of EMAA onto a single reinforcing ply, additional layers of 8H satin reinforcement were placed above and below the central ply to produce symmetrically stacked preforms with EMAA along the midplane. The complete details of stacking sequences (including those with resistive heater interlayers) for specific test geometries can be found in respective sections.

Melt consolidation of preforms containing printed EMAA was accomplished by placing the preform between a pair of aluminum plates (length \times width \times thickness: 405 \times 405 \times 6.35 mm) with additional weights applied to produce a static pressure of 1 kPa relative to the surface area (length \times width). The preform/plate assembly was heated in a mechanical convection oven (OF-22, Cole-Parmer, Inc.) from RT to 110 $^\circ\text{C}$ over 15 min. The temperature was held for 75 min and then reduced to 60 $^\circ\text{C}$ over 90 min, prior to removing the assembly from the oven and allowing it to cool down to RT.

2.3. Vacuum-Assisted Resin Transfer Molding (VARTM)

Prior to vacuum-assisted infusion of the preforms, epoxy resin (Araldite 8605, Huntsman Advanced Materials, LLC) and amine hardener (Aradur 8605, Huntsman Advanced Materials, LLC) were mixed in a 100:35 resin to hardener ratio by weight and degassed for 2 h at RT under 12 Torr abs vacuum within a drying oven (ADP 300C, Yamato, Inc.). Vacuum Assisted Resin Transfer Molding (VARTM) was conducted at 2 Torr (abs) until complete fabric wetting, at which point the vacuum was decreased to 380 Torr (abs) for 24 h at RT until matrix solidification. The resulting FRP composite plates were cured for 2 h

at 121 $^\circ\text{C}$ followed by 2 h at 150 $^\circ\text{C}$ to yield a final glass-transition temperature (T_g) of approximately 145 $^\circ\text{C}$ as measured by dynamic mechanical analysis (DMA).

2.4. Thermomechanical characterization

2.4.1. Tension specimen fabrication

Plain composite tension samples (≈ 4 mm thick) comprise sixteen 8H satin E-glass plies in an alternating sequence of $[90/0]_8$, where the lamina angle corresponds to the warp direction of the woven reinforcement with respect to the fracture propagation direction (i.e., 0°). EMAA-modified composites contain a melt consolidated EMAA midplane interlayer with a stacking sequence of $[90/0]_4$ -EMAA- $[90/0]_4$. EMAA patterns were printed at 36% areal coverage, a trace width (w) of 500 μm , and a thickness (t) of 300 μm in both longitudinal (L) and transverse (T) orientations. The highest 36% areal coverage (≈ 2 vol%) was selected to represent a worst-case scenario (i.e., greatest potential detriment to structural integrity). Preforms were infused via VARTM and cured. Samples 20 mm wide and 254 mm long were sectioned from the composite panel using a diamond blade wet saw. Four full width and 45 mm long fiberglass tabs were bonded to both ends of the front and back faces of each specimen using a structural adhesive (DP460NS, 3M), which was cured at RT for 24 h and then 49 $^\circ\text{C}$ for 4 h to attain full bond strength (as recommended by the manufacturer). Front and back sample surfaces between the tabs were painted matte white and then speckled black to provide sufficient contrast for Digital Image Correlation (DIC) during mechanical evaluation.

2.4.2. In-plane tension testing

Uniaxial in-plane tension testing was conducted according to ASTM D3039 on an electromechanical load frame (Exceed E45, MTS Inc.) equipped with mechanical wedge grips and a 100 kN load cell. Quasi-static displacement-controlled loading was applied at a crosshead rate of 1.5 mm/min while concurrent images for DIC were acquired on the front and back of each sample using two 12.3 MP machine vision cameras (GS3-U3-123S6M-C, Teledyne FLIR, Inc.). Full-field strains were calculated on each observed face using Vic-2D software (Correlated Solutions, Inc.) and compared against each other to ensure no loading eccentricity (i.e., bending) during testing.

2.4.3. Flexure specimen fabrication

Plain composite flexure samples (≈ 2 mm thick) comprised eight woven E-glass plies in a stacking sequence of $[90/0]_4$, while samples with printed EMAA patterns had a stacking sequence of $[90/0]_2$ -EMAA- $[90/0]_2$. Longitudinal (L) patterns were printed at areal coverages of 12, 24, and 36%, a trace width (w) of 500 μm , and a thickness (t) of 150 μm to produce the same maximum EMAA percentage (≈ 2 vol%) as the 36% areal coverage tension samples. Following melt consolidation, VARTM, and curing, individual samples were sectioned to 12.5 mm wide by 60 mm long using a diamond blade wet saw.

2.4.4. Dynamic Mechanical Analysis (DMA)

DMA in 3-pt flexure (50 mm span length) was performed according to ASTM E1640. A Q800 dynamic mechanical analyzer (TA Instruments, Inc.) applied an initial preload of 0.01 N to each sample, followed by an oscillating strain of 0.1% at 1 Hz frequency. A temperature sweep from RT to 250 $^\circ\text{C}$ was conducted at a ramp rate of 5 $^\circ\text{C}/\text{min}$ while storage modulus (E'), loss modulus (E''), and $\tan(\delta)$ — (i.e., the ratio of E'' to E') — were collected at a sampling rate of 0.5 Hz. We report the peak of $\tan(\delta)$ as the T_g for each sample.

2.5. Mode-I fracture characterization

2.5.1. Fracture specimen fabrication

Plain composite fracture samples (≈ 4 mm thick) comprised sixteen woven E-glass plies in an alternating sequence of $[90/0]_8$, while EMAA-modified composites had a stacking sequence of $[90/0]_4$ -EMAA- $[90/0]_4$. Patterns were printed at 12, 24, and 36% as-printed areal coverages and varying thicknesses (t) of 150, 300, and 450 μm with a constant target trace width (w) of 500 μm . Patterns were printed in both longitudinal (L) and transverse (T) orientations with respect to crack propagation. A 25 μm thick ethylene tetrafluoroethylene (ETFE) film (full panel width and 50 mm long) was placed at the midplane of each preform to serve as the pre-crack.

Following melt consolidation, VARTM, and curing, samples 25 mm wide by 140 mm long were sectioned from the composite plate using a diamond-blade wet saw. Steel hinges were bonded to the outer composite faces on the pre-crack end with structural adhesive and cured at RT for 24 h following an additional 4 h at 49 $^\circ\text{C}$. Straight lines marked on the bottom and side faces in 5 mm increments (to a total distance 50 mm from the interior edge of the ETFE film) designate measurement points for crack length determination.

2.5.2. Mode-I fracture testing

Double-cantilever beam (DCB) mode-I fracture tests were conducted in accordance with ASTM D5528 using a 10 kN electromechanical load frame (Alliance RT/5, MTS, Inc.), equipped with a 250 N load cell. Displacement-controlled loading of the DCBs was performed at a crosshead rate of 5 mm/min to propagate a delamination from the pre-crack along the midplane of the sample, shown in Fig. 2a. A 4K resolution webcam (Logitech BRIO), equipped with a custom macro lens (LM12JC5M2, Kowa Optical Products Co., Ltd.), was used to monitor crack growth from the top surface of translucent glass-fiber composites. A backlight (MI-150, Dolan-Jenner, Inc.) placed below

enhanced contrast between the crack front and undamaged regions during testing. Fig. 2b shows a typical load–displacement curve from a DCB fracture test of a plain GFRP composite. The sample largely exhibited linear elastic behavior as it was loaded to the crack initiation point, after which the crack was propagated to a length of $\Delta a = 50$ mm, before unloading.

2.5.3. Fracture quantification

Fracture resistance was quantified via mode-I critical strain energy release rate (G_{IC}) (i.e., the amount of energy required to create opposing crack surfaces of unit area). In this study, (G_{IC}) was calculated using both modified beam theory (MBT) and the area method [59]. For MBT, G_{IC} values were computed at crack growth increments of 5 mm from the edge of the pre-crack film ($\Delta a = 0$ mm) to a total propagation length ($\Delta a = 50$ mm) using the following equation:

$$G_{IC} = \frac{3P\delta}{2b(a + |\Delta|)}, \quad (1)$$

where P is the force resulting from an applied displacement δ , b is the sample width, and $a = (a_0 + \Delta a)$ is the total crack length, a_0 is the distance from the loading plane to the front edge of the pre-crack (≈ 47.5 mm), and Δa is the linear distance of crack propagation. In Eq. (1), Δ is a correction factor to account for non-zero rotation of the DCB arms at the delamination front [59]. A resistance curve (R-curve) is constructed by plotting the discrete MBT G_{IC} values at 5 mm crack propagation lengths (Δa). A representative R-curve for a plain composite is shown in Fig. 2c where a nearly constant G_{IC} is observed throughout delamination, indicating steady fracture behavior due to mid-plane warp tow alignment with the crack propagation direction.

In contrast to the MBT approach that quantifies G_{IC} across multiple crack length measurements, the area method calculates a single G_{IC} value for the entire fracture surface according to:

$$G_{IC} = \frac{1}{b} \frac{\Delta U}{\Delta a}, \quad (2)$$

where ΔU is the energy required to create opposing crack surfaces of incremental area ($b\Delta a$) and defined by the area enclosed with the entire load–displacement curve:

$$\Delta U = \int_0^{\delta} P \, d\delta \Big|_{\Delta a}. \quad (3)$$

Fig. 2c shows G_{IC} calculated via the area method for a typical plain composite sample, represented as a solid horizontal line, where this singular value of 409 J/m^2 is in good agreement with the steady state propagation value of $\approx 409 \pm 6$ J/m^2 calculated by MBT (dashed line). Optical microscope images and a complementary scanning electron micrograph (SEM) inset in Fig. 2c reveal the fracture surface topology (i.e., matrix debonded from fibrous reinforcement) of a plain GFRP laminate. A clear dichotomy in morphology is observed between the fiber- and matrix-rich surfaces on either side of the delamination.

2.6. In situ thermal remending

2.6.1. Self-healing fracture specimen fabrication

DCB samples with *in situ* self-healing capabilities were manufactured using a sixteen-layer preform similar to the EMAA-modified fracture specimens, except the 5th and 12th layers of E-glass fabric were replaced with resistive heater textiles (LaminaHeat, LLC) 254 mm wide and 140 mm long. Prior to layup, each resistive heating ply was marked along two continuous rows of copper bus bars at each end to delineate centerline locations of eight DCB samples. A steel razor blade was used to perforate the top of the E-glass shroud enclosing the bus bars along the sample centerlines, creating a ≈ 15 mm long slit from the outer edges. The perforations were first coated with conductive silver paint, then dried for 30 min before placing a ≈ 25 mm long segment of copper wire (0.81 mm diameter) onto each slit with ≈ 10 mm overhang, and finally applying a silver paint

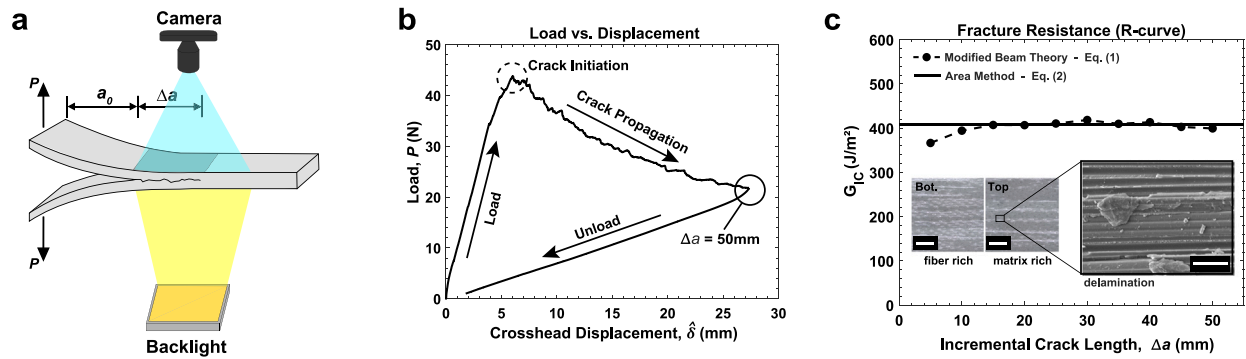


Fig. 2. Mode-I fracture evaluation (a) A schematic of a double cantilever beam (DCB) test with backlight and overhead camera for crack tracking. (b) A representative load-displacement curve for a plain glass-fiber composite DCB with a propagated delamination (Δa) of 50 mm. (c) A representative R-curve (i.e., critical strain energy release rate (G_{IC}) as a function of incremental crack length) for the specimen in (b) with multiple data points calculated at 5 mm crack growth increments from modified beam theory (Eq. (1)) and one singular value (solid line) for the entire delamination via the area method (Eq. (2)). Inset images show the two opposing midplane fracture surfaces with largely differing topology (scale bar = 5 mm) and a scanning electron micrograph from a delamination region exhibiting both features of fiber-matrix debonding (scale bar = 25 μ m).

overcoat. After an additional 30 min of drying, the electrically connected section was potted with a thin layer of structural adhesive (DP460NS), secured using a single layer of conductive copper tape, and cured at 49 °C for 4 h. The prepped heaters were then incorporated into the EMAA-modified preform with a stacking sequence of [0/90]₂-heater-[0/90/0]-EMAA-[90/0/90]-heater-[0/90]₂. The preform then undergoes the same melt consolidation, VARTM, curing, and fabrication as described for previous DCB samples.

Once the self-healing DCB samples (25 mm wide \times 140 mm long) are sectioned from the composite plate, each specimen has four exposed cross-sections of embedded copper wire (0.81 mm diameter), two at each end (i.e., length = 0 and 140 mm). A 0.65 mm diameter center hole was drilled 4 mm deep into each embedded wire and another copper wire (0.64 mm diameter) was inserted into each hole. The external surface of the press-fit wire connection was reinforced with a 5 min epoxy and allowed to sit for 24 h at RT to develop sufficient bonding strength. These wired connections enable electrical power delivery to achieve *in situ* resistive (i.e., Joule) heating. The top face of each self-healing DCB sample was painted matte black for infrared (IR) imaging during testing.

2.6.2. Self-healing characterization

In situ self-healing via thermal remending was performed within the load frame after propagating a 50 mm delamination through the composite midplane and unloading to zero crosshead displacement. A DC power supply (PWS4602, Tektronix, Inc.) provided electrical power (10.5–12.5 W) to the embedded resistive heaters commencing *in situ* thermal remending. The target maximum top surface healing temperatures ($T_h = 110, 130$ °C) were attained in roughly 5 min as monitored by an overhead IR camera (A600, Teledyne FLIR, Inc.) and power was applied for a total of 15 min before disconnecting and allowing the specimen to cool for 30 min to RT. *In situ* thermal remending temperatures remained below the T_g of the epoxy matrix (≈ 145 °C). A total of ten fracture-heal cycles were performed for each sample configuration.

Healing efficiency ($\hat{\eta}$) is defined as the ratio between healed and virgin critical strain energy release rates [28] and when expressed as a percentage takes the following form:

$$\hat{\eta} = \frac{G_{IC}^{\text{healed}}}{G_{IC}^{\text{virgin}}} \times 100\%, \quad (4)$$

where G_{IC}^{virgin} and G_{IC}^{healed} are the virgin and healed critical strain energy release rates calculated via the area method, respectively.

2.7. Topological characterization of fracture surfaces

Optical and scanning electron microscopy were employed to characterize fractured composite surface morphologies. Optical images were acquired with a digital light microscope (AXIO Zoom V.16, Zeiss, Inc.) equipped with an LED ring light for top surface illumination. Scanning electron micrographs were acquired with a variable pressure scanning electron microscope (S3200N, Hitachi, Ltd.) at a 10 kV accelerating voltage after sputtering samples with gold/palladium to a target coating thickness of ≈ 10 nm.

3. Results

3.1. In-plane tensile and thermomechanical response

We examine the suitability of EMAA-toughened laminates for stiffening and strength critical applications by comparing the in-plane tensile response to plain (i.e., unmodified) composites. Fig. 3a shows representative bilinear stress-strain curves with almost no discernible difference between EMAA-modified composites at the highest 36% areal coverage considered in this study (≈ 2 vol%) when compared to the plain composite laminates (see Table A.1). Also, pattern orientation with respect to the loading direction—longitudinal (L) and transverse (T)—does not appear to significantly alter the in-plane tensile response. Fig. 3b corroborates these stress-strain observations, with less than 5% difference in initial/final moduli and ultimate tensile strength for each EMAA sample type in reference to plain GFRP laminates. As shown in our prior work [58], the embedded resistive heaters have a more pronounced effect on in-plane tensile properties than printed EMAA patterns at these volume fractions.

In addition to retention of mechanical properties at ambient conditions, assessing the thermomechanical effects of EMAA inclusions in GFRP laminates is important given that *in situ* self-healing requires retention of structural integrity throughout the thermal remending process. To this end, the glass-transition temperature (T_g) and elastic storage modulus (E') evolution of plain composites and laminates containing EMAA patterns are assessed using dynamic mechanical analysis (DMA). Fig. 3c shows that the inclusion of EMAA at the highest 36% areal coverage has a negligible effect on the measured T_g compared to a plain composite, with a value of ≈ 145 °C in both cases. The values of E' at RT and at T_g for samples with patterns at 12, 24, and 36% areal coverage are shown in Fig. 3d. Commensurate with the tensile testing results, less than 5% difference in E' is observed at either temperature for all sample types. Thus, we conclude that for the EMAA loadings and patterns considered, the in-plane tensile and thermomechanical response is nearly the same to that of plain GFRP composites.

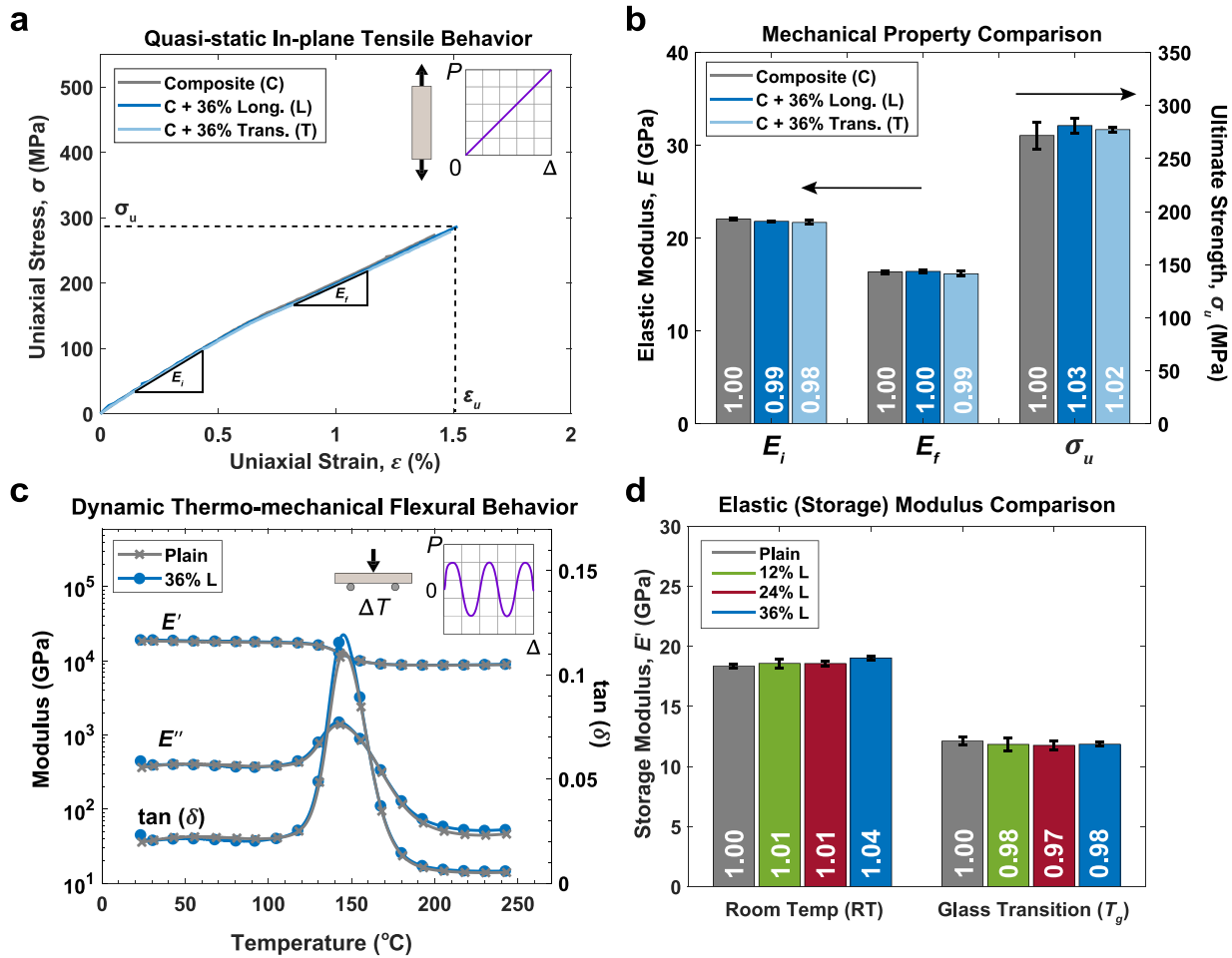


Fig. 3. In-plane tensile and thermomechanical behavior. (a) Representative ambient tensile stress–strain curves for plain GFRP composites and laminates modified with EMAA interlayers in either longitudinal (L) or transverse (T) orientations at 36% as-printed areal coverage. (b) Comparative tensile summary of plain versus patterned composites’ initial elastic modulus (E_i), final elastic modulus (E_f), and ultimate tensile strength (σ_u); numbers at the bottom of bar plots indicate the normalized property values with respect to plain composites. Error bars represent the standard deviation from the mean ($n = 5$). (c) Thermo-mechanical evolution of storage modulus (E'), loss modulus (E''), and $\tan(\delta)$ measured via DMA for plain GFRP and composites containing an EMAA midplane layer at the maximum 36% areal coverage. (d) Comparative elastic storage modulus summary of plain and EMAA-modified composites at room temperature (RT) and the T_g of the host matrix ($\approx 145^\circ\text{C}$); numbers at the bottom of bar plots indicate the normalized storage modulus values with respect to plain composite at each respective temperature. Error bars represent the standard deviation from the mean ($n = 3$).

3.2. Mode-I fracture behavior

As depicted in Fig. 4a, 3D-printed (and melt-bonded) EMAA interlayers are expected to improve GFRP interlaminar delamination resistance by forcing a cohesive fracture (as opposed to adhesive) through the tough and ductile EMAA domains. Based on prior work [12] showing that adhesive versus cohesive fracture behavior is influenced by thermoplastic interlayer thickness, DCB samples with 150, 300, and 450 μm printed EMAA patterns (longitudinal orientation at 24% areal coverage) are evaluated. Fig. 4b compares mode-I strain energy release rate (G_{IC}), i.e., fracture resistance, versus as-printed thickness. The thinnest (150 μm) configuration results in the lowest G_{IC} of $580 \pm 14 \text{ J/m}^2$, roughly half that of the thicker 300 and 450 μm EMAA interlayers, which have nearly equivalent (within 5%) G_{IC} values of $1230 \pm 128 \text{ J/m}^2$ and $1170 \pm 22 \text{ J/m}^2$, respectively. Topological investigation of the fracture surfaces reveals largely adhesive failure for the 150 μm pattern, characterized by a majority of EMAA retained on one half of the DCB samples. In contrast, the two thicker interlayers exhibit cohesive fracture where EMAA is retained on both halves of the DCB samples. The larger print thicknesses may favor cohesive failure not only due to increased crack tortuosity, but also a greater volume of EMAA for incorporation and anchoring into the micro-textured reinforcement during melt consolidation (see Fig. A.1). These results reveal a threshold as-printed thickness to achieve cohesive failure of

the EMAA domains, which is ideal from both a toughening and healing perspective. Since the two thicker patterns have statistically equivalent fracture resistance (G_{IC}), the lower 300 μm thickness is selected for all subsequent evaluations as it represents the lowest volume fraction ($\approx 0.7\text{--}2.1 \text{ vol}\%$ depending on areal coverage) thus better preserving other structural performance metrics.

Upon selecting an ideal pattern thickness, the effect of EMAA areal coverage and orientation on interlaminar fracture are investigated. Representative load–displacement curves for plain DCB samples and those with EMAA midlayers printed at 12, 24, and 36% areal coverage in both longitudinal (L) and transverse (T) orientations are shown in Fig. 4b. Significant toughening compared to a plain composite is evident from the load–unload curves where EMAA-modified composites encompass more area (Eq. (3)), which increases with an increase in areal coverage. Printed pattern orientation with respect to the crack propagation direction (L vs. T) has a lesser effect on the global fracture energy evidenced by relatively small differences in load–displacement area, which further diminishes at higher areal coverages. However, orientation does affect the local fracture response, clearly shown by the longitudinal (L) and transverse (T) load–displacement curves at 12% areal coverage. For the longitudinal pattern, steady crack propagation occurs with a smooth decline in measured load as the crack grows. The crack front shown at the bottom of Fig. 4d maintains a characteristic

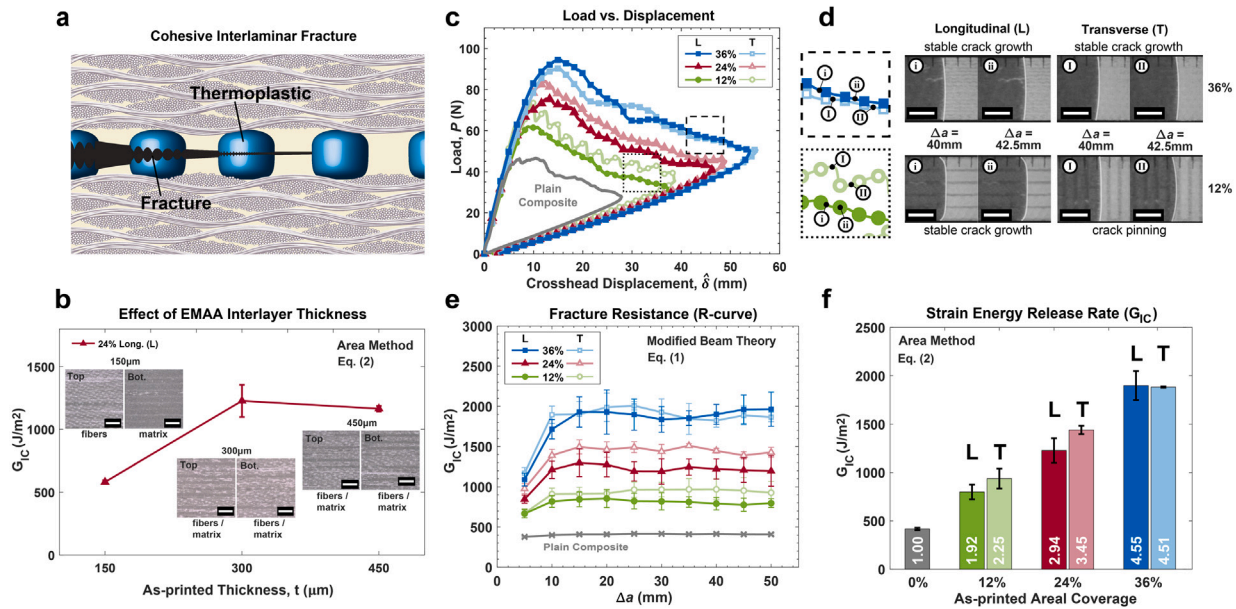


Fig. 4. Interlaminar fracture toughening. (a) A depiction of the desired cohesive failure of printed thermoplastic (EMAA) domains to provide interlaminar fracture toughening. (b) Critical strain energy release rate (G_{IC}) for composites with varying as-printed EMAA interlayer thicknesses (150, 300, and 450 μm) in a longitudinal (L) pattern at 24% areal coverage. Inset optical images show representative fracture surfaces from top/bottom halves of tested DCB samples (scale bar = 5 mm). (c) Representative load-displacement curves for plain GFRP composites and laminates containing longitudinal (L) and transverse (T) EMAA midplane patterns at 12%, 24%, and 36% as-printed areal coverage. (d) Crack propagation behavior at specific locations in (c) showing crack front shape for longitudinal and transverse pattern orientations at 12% and 36% areal coverage (scale bars = 10 mm). (e) Fracture resistance (R-curves) for respective samples in (c) that are constructed using modified beam theory. (f) G_{IC} values for respective samples in (c) calculated via the area method; numbers at the bottom of bar plots indicate the normalized G_{IC} values with respect to plain composites. Error bars in (b), (e), and (f) represent the standard deviation from the mean ($n = 3$).

parabolic (i.e., “thumb-nail”) shape throughout propagation [60]. Conversely, the load–displacement curve for transverse (T) 12% pattern exhibits a stick–slip behavior [61,62], as indicated by the rise and fall of the measured load as the crack grows. The correlated crack front images in Fig. 4d show that the peaks correspond to the crack front flattening (i.e., blunting) as the crack interacts with a transverse printed trace, while the valleys correlate to steady crack propagating through the plain composite sections between traces with a similar thumb-nail shape observed for longitudinal (L) patterns. The differences in local propagation behavior are less prevalent with increasing areal coverage, i.e., nearly identical behavior is displayed at the 36% areal coverage between the longitudinal and transverse orientations. As shown in Fig. 4c for 36% samples, a relatively smooth decline in load with crack growth is noted for both pattern orientations, with Fig. 4d showing a consistent parabolic crack front profile.

Representative fracture resistance curves (i.e., R-curves) for each sample type are shown in Fig. 4e that are calculated via modified beam theory (Eq. (1)) at 5 mm crack growth increments (Δa) through the entire 50 mm delamination. The R-curves for all samples initially increase, but after reaching $\Delta a = 10$ mm they plateau, at which point the crack growth rate becomes steady. Fig. 4f provides a comparative summary of G_{IC} calculated via the area method (Eq. (2)) versus pattern areal coverage, which is the dominant parameter for the amount of toughening attained. Composites with 36% EMAA areal coverage exceed a 450% increase in fracture resistance compared to plain laminates with a G_{IC} of $420 \pm 13 \text{ J/m}^2$. A nearly linear increase in G_{IC} with increased areal coverage is observed, with the transverse patterns exhibiting a slight increase over longitudinal orientations that diminishes with increased areal coverage and becomes statistically indistinguishable at 36%.

3.3. In situ self-healing

Following investigation of EMAA fracture toughening behavior, similarly patterned DCBs—yet now containing resistive heaters for *in situ* self-healing via thermal-remending (Fig. 5a)—are evaluated to study

the effect of EMAA areal coverage and orientation on healing efficiency. Fig. 5b shows a representative top surface temperature profile of a DCB in the load frame during *in situ* healing ($T_h = 130 \text{ }^\circ\text{C}$) where fairly uniform heating is achieved across the entire delamination region ($\Delta a = 50 \text{ mm}$). Since the IR camera only captures surface temperature, we resorted to finite element (FE) modeling to ensure that the temperature in the interior also remains below T_g at the target input power (12 W). Figure S2 compares the results from a 3D FE heat transfer simulation with experimental 2D measurements, which match well. The numerical results reveal that, at steady-state, the average measured top surface temperatures and simulated midplane temperatures are within $5 \text{ }^\circ\text{C}$ of each other in the 50 mm fracture/healing region, and below T_g , whereby the composite can maintain elastic modulus during repair; a key attribute for real-world translation. DCB samples with midplane EMAA patterns at 12, 24, and 36% as-printed areal coverages in both longitudinal and transverse orientations are evaluated for an initial virgin (V) fracture and 10 subsequent healing (H) cycles. Fig. 5c shows representative load–displacement curves from each areal coverage and orientation for the virgin, heal 1, heal 5, and heal 10 DCB tests. The shaded regions depict evolving load–displacement envelopes as the healed fracture resistance (G_{IC}) increases and eventually converges by heal 10. This observed growth in healed fracture resistance is attributed to the spreading of the EMAA over multiple healing cycles due to physical and chemical effects [56,57] and sustained cohesive failure of the EMAA domains [58]. For 36% transverse (T) samples, out-of-midplane delamination is observed due to excessive midplane fracture resistance relative to neighboring layers. Further testing for such samples is not continued, but indicates there is an upper limit to toughening/healing before other failure modes occur. While longitudinal (L) samples of all areal coverages display smooth load–displacement behavior in both the virgin and healed cycles, transverse (T) patterns only display stick–slip behavior in the virgin cycle where such behavior is suppressed by EMAA domains after spreading from thermal-remending.

Fig. 5d shows critical strain energy release rates and healing efficiencies corresponding to virgin (testing cycle 0) and ten healing

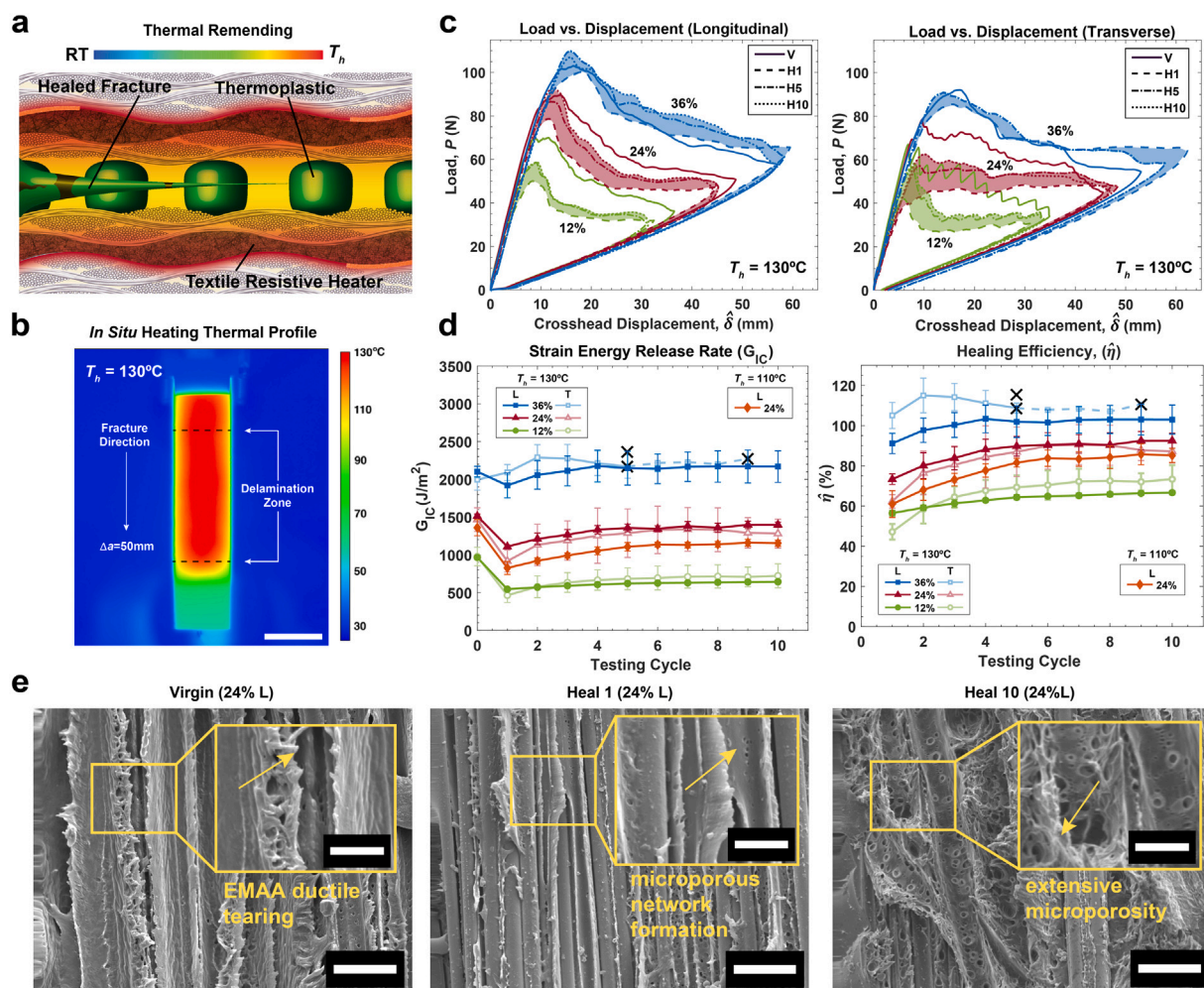


Fig. 5. *In situ* self-healing. (a) A depiction of self-healing via *in situ* thermal remending where embedded resistive heaters provide thermal energy for melting, flow, and dynamic re-bonding of printed thermoplastic (EMAA) domains. (b) Top surface temperature distribution of a DCB specimen heated in the load frame to a target healing temperature of 130°C as measured via an overhead infrared camera (scale bar = 25 mm). (c) Representative load–displacement curves for virgin (V), heal 1 (H1), heal 5 (H5), and heal 10 (H10) DCB specimens containing longitudinal (L) or transverse (T) EMMA serpentine patterns at 12%, 24%, and 36% areal coverage. The shaded regions envelope heal cycles 1–10 for all configurations except for the transverse (T) 36% samples which envelope heal cycles 1–5. (d) Summary of critical strain energy release rate (G_{IC}) and healing efficiency (η) as a function of testing cycle (black X's for transverse (T) 36% samples indicate occurrence of out-of-plane delamination for 2/3 samples after heal 5 and for remaining 1/3 sample after heal 9). Error bars represent the standard deviation from the mean ($n = 3$). (e) Scanning electron micrographs (SEM) illustrating the evolution in fracture surface topology after the virgin fracture (left), heal 1 (middle), and heal 10 (right) for a 24% longitudinally patterned specimen (scale bars = 25 μm , inset scale bars = 10 μm).

cycles. Akin to the prior toughening study, pattern areal coverage has a dominant effect on self-healing performance, with healing efficiencies reaching 60, 85, and 100% for patterns at 12, 24, and 36% coverage, respectively. Note, healing efficiencies (Eq. (4)) are calculated with respect to the toughened virgin (G_{IC}) values, signifying that complete recovery of enhanced fracture resistance is possible. Thermal remending at a target temperature of $T_h = 110^\circ\text{C}$ is also achieved with minor impact on healing performance compared to 130°C since this lower temperature is still well above the melting point of the EMMA studied ($T_m \approx 85^\circ\text{C}$) [58]. Healing at 110°C , which is further below T_g of the epoxy matrix ($\approx 145^\circ\text{C}$), is better suited to preserve elastic modulus during repair (Table A.2). Additionally, two types of control samples were evaluated: (i) *in situ* heated but not containing any EMMA, (ii) non-heated and containing EMMA printed at 36% areal coverage. Neither type of control sample exhibited any measurable fracture recovery (see Supporting Information).

Scanning electron micrographs in Fig. 5e reveal the mechanisms driving self-healing performance. In early cycles (i.e., virgin and heal 1), fracture surfaces show evidence of ductile cohesive fracture (tearing) of EMMA and the formation of microporosity in the thermoplastic as a result of aforementioned and previously studied condensation

reactions between EMMA and the epoxy matrix. These pressurizing reactions assist in the spreading of molten EMMA to increase areal coverage and crack tortuosity, thereby increasing fracture resistance with further cycling. By heal cycle 10, a densely connected microporous network is apparent as the healing efficiency appears to converge. As demonstrated in [58], sustained healing performance extends well beyond the cessation of covalent/ionic reactions (and corresponding disappearance of the microporous network) where continued hydrogen bonding between cohesively-fractured EMMA domains provides the capacity for prolonged recovery (up to 100 heal cycles) of interlaminar fracture resistance. Here we have shown that EMMA interlayer thickness plays a critical role in producing cohesive failure, essential for repeated repair. An as-printed thickness of 300 μm and above is sufficient post composite fabrication to achieve cohesive fracture of EMMA domains. Also, we reveal that printed areal coverage is largely responsible for the amount of fracture toughening and self-healing, while pattern orientation with respect to crack direction plays a minor role—further diminishing with higher areal coverage and continued fracture cycling. In other words, given sufficient density of printed healing agent, interlaminar toughening and self-healing is fairly agnostic to crack direction (at least for serpentine patterns),

thus providing flexibility in multifunctional composite design. EMAA amount and placement must also be considered in the context of other structural properties (e.g., flexure), providing an opportunity for future investigations.

4. Closure

This article presents a glass fiber-reinforced polymer (GFRP) composite system with tailored toughening and *in situ* self-healing capabilities—two attractive attributes for combating delamination, which often curtails the service lifetime of laminated composite structures. Our approach leverages additive manufacturing to 3D-print commodity thermoplastic (EMAA) interlayers, achieving a 450% increase in delamination resistance while limiting changes (< 5%) to ambient in-plane tensile and also thermomechanical properties with respect to unmodified composites. Notably, the repeatable *in situ* self-healing—achieved via thermal remending of cohesively fractured EMAA domains—manifests below the T_g of the FRP laminate. The paper details a systematic study that unravels how printed pattern design variables affect toughening and healing responses. EMAA areal density largely governs the delamination resistance and overall healing performance. On the other hand, pattern orientation plus areal density control local crack propagation near pattern elements: increasing areal density or spreading of material during healing suppresses stick-slip fracture behavior in transversely patterned samples. Further, our studies indicate that *in situ* self-healing performance does not degrade even after ten fracture–heal cycles.

The developed material system offers a promising and economical solution to mitigate catastrophic damage in fiber composites, thus enabling service life extension of corresponding structures, especially those in demanding and inaccessible environments or otherwise difficult to repair/replace. A plausible future work could develop a mechanics-based modeling framework to gain a deeper understanding of the multi-scale fracture and multi-physics self-healing behaviors of this new class of FRP composites.

CRediT authorship contribution statement

Jack S. Turicek: Investigation, Formal analysis, Visualization, Writing. **Alexander D. Snyder:** Investigation, Formal analysis, Visualization, Writing. **Kalyana B. Nakshatrala:** Formal analysis, Writing. **Jason F. Patrick:** Conceptualization, Methodology, Data Curation, Supervision, Project administration, Funding acquisition, Writing.

Declaration of competing interest

The authors declare the following financial interests/personal relationships which may be considered as potential competing interests: The authors declare no personal relationships that could have appeared to influence the work reported in this paper. The self-healing composite system presented in this work has been issued a US Patent (No. 11,613,088 B2) with J.F.P. and A.D.S. as listed inventors. The remaining authors declare no competing intellectual property interests.

Data availability

Data will be made available on request

Acknowledgments

The authors acknowledge the financial support from the Strategic Environmental Research and Development Program (SERDP), USA through grant No. W912HQ21C0044 awarded to J.F.P. The work was performed in part at the Analytical Instrumentation Facility (AIF) at North Carolina State University, which is supported by the State of North Carolina and the National Science Foundation (grant ECCS-2025064). We thank Zachary J. Phillips for assistance with thermal data analysis and visualization.

Appendix A

See Fig. A.1, Tables A.1 and A.2.

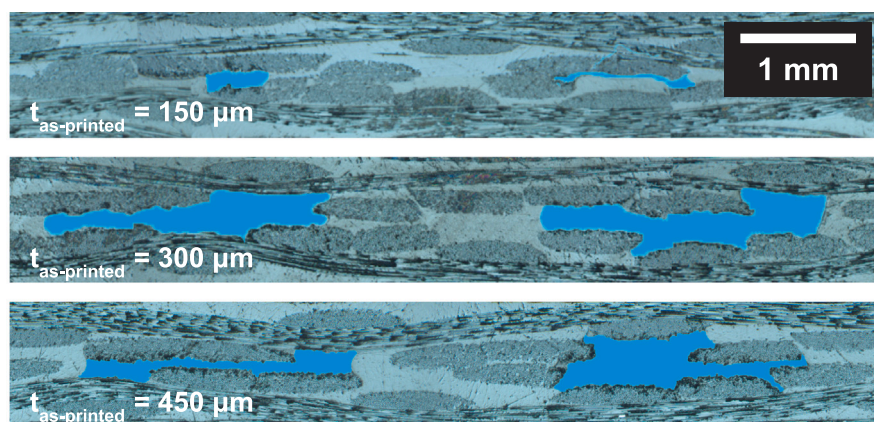


Figure. A.1. EMAA thickness variation. Tiled optical micrographs of GFRP composite cross-sections for 24% EMAA at varying as-printed thicknesses (150, 300, and 450 μm) showing different EMAA melt-bonding morphologies (blue overlay) resulting from respective placement between fiber-tows.

Table. A.1
3D-printed EMAA and respective manufactured fiber-composite properties.

As-printed areal coverage (%)	As-printed thickness (μm)	Composite thickness (mm)	EMAA volume fraction (%)
12	300	3.95 ± 0.03	0.716
24	150	3.98 ± 0.02	0.710
24	300	3.96 ± 0.01	1.428
24	450	3.98 ± 0.02	2.131
36	300	3.99 ± 0.02	2.125

Table. A.2
Thermomechanical properties, mode-I fracture resistance, and healing performance of GFRP composites.

As-printed areal coverage (%)	E' , RT (GPa)	E' , 110 °C (GPa)	E' , 130 °C (GPa)	E' , T_g (GPa)	G_{IC} , V (J/m ²)	G_{IC} , H1 (J/m ²)	G_{IC} , H5 (J/m ²)	G_{IC} , H10 (J/m ²)
0	18.4 ± 0.16	17.4 ± 0.14	16.0 ± 0.15	12.1 ± 0.31	417 ± 10	–	–	–
^a 12	18.6 ± 0.37	17.4 ± 0.24	15.8 ± 0.49	11.9 ± 0.52	965 ± 21	545 ± 2	621 ± 17	643 ± 17
^a 24	18.6 ± 0.21	17.4 ± 0.10	15.7 ± 0.37	11.8 ± 0.37	1513 ± 27	1109 ± 21	1357 ± 51	1398 ± 35
^b 24	–	–	–	–	1359 ± 107	826 ± 85	1107 ± 56	1154 ± 41
^a 36	19.0 ± 0.17	17.7 ± 0.20	16.0 ± 0.25	11.9 ± 0.18	2102 ± 70	1919 ± 165	2147 ± 223	2169 ± 209

As-printed pattern thickness = 300 μm.

^aHealing conducted at 130 °C.

^bHealing conducted at 110 °C.

Appendix B. Supplementary data

Supplementary material related to this article can be found online at <https://doi.org/10.1016/j.compscitech.2023.110073>.

References

- [1] M.R. Wisnom, The role of delamination in failure of fibre-reinforced composites, *Phil. Trans. R. Soc. A* 370 (1965) (2012) 1850–1870.
- [2] W.J. Cantwell, J. Morton, The significance of damage and defects and their detection in composite materials: A review, *J. Strain Anal. Eng. Des.* 27 (1) (1992) 29–42.
- [3] B. Wang, S. Zhong, T.-L. Lee, K.S. Fancey, J. Mi, Non-destructive testing and evaluation of composite materials/structures: A state-of-the-art review, *Adv. Mech. Eng.* 12 (2020) 1–28.
- [4] K.B. Katnam, L.F.M. Da Silva, T.M. Young, Bonded repair of composite aircraft structures: A review of scientific challenges and opportunities, *Prog. Aerosp. Sci.* 61 (2013) 26–42.
- [5] R.B. Heslehurst, *Engineered Repairs of Composite Structures*, first ed., CRC Press / Taylor & Francis, Boca Raton, 2019.
- [6] A. Kinloch, S. Shaw, D. Tod, D. Hunston, Deformation and fracture behaviour of a rubber-toughened epoxy: 1. Microstructure and fracture studies, *Polymer* 24 (10) (1983) 1341–1354.
- [7] S.V. Nair, A. Subramaniam, L.A. Goettler, Fracture resistance of polyblends and polyblend matrix composites: Part II Role of the rubber phase in Nylon 6,6/ABS alloys, *J. Mater. Sci.* 32 (1997) 5347–5354.
- [8] J.H. Hodgkin, G.P. Simon, R.J. Varley, Thermoplastic toughening of epoxy resins: a critical review, *Polym. Adv. Technol.* 9 (1) (1998) 3–10.
- [9] S. Awang Ngah, A.C. Taylor, Toughening performance of glass fibre composites with core-shell rubber and silica nanoparticle modified matrices, *Composites A* 80 (2016) 292–303.
- [10] I. Chang, J. Lees, Recent development in thermoplastic composites: a review of matrix systems and processing methods, *J. Thermop. Compos. Mater.* 1 (3) (1988) 277–296.
- [11] S.K. Bhudolia, P. Perrotey, S.C. Joshi, Mode I fracture toughness and fractographic investigation of carbon fibre composites with liquid Methylmethacrylate thermoplastic matrix, *Composites B* 134 (2018) 246–253.
- [12] S. Matsuda, M. Hojo, S. Ochiai, A. Murakami, H. Akimoto, M. Ando, Effect of ionomer thickness on mode I interlaminar fracture toughness for ionomer toughened CFRP, *Composites A* 30 (1999) 1311–1319.
- [13] N. Sela, O. Ishai, L. Banks-Sills, The effect of adhesive thickness on interlaminar fracture toughness of interleaved CFRP specimens, *Composites* 20 (1989) 257–264.
- [14] N. Vallack, W.W. Sampson, Materials systems for interleave toughening in polymer composites, *J. Mater. Sci.* 57 (2022) 6129–6156.
- [15] H.J. Sue, R.E. Jones, E.I. Garcia-Meitin, Fracture behaviour of model toughened composites under Mode I and Mode II delaminations, *J. Mater. Sci.* 28 (1993) 6381–6391.
- [16] M. Yasaee, I.P. Bond, R.S. Trask, E.S. Greenhalgh, Mode I interfacial toughening through discontinuous interleaves for damage suppression and control, *Composites A* 43 (2012) 198–207.
- [17] N. Sela, O. Ishai, Interlaminar fracture toughness and toughening of laminated composite materials: a review, *Composites* 20 (1989) 423–435.
- [18] A. Cohades, C. Branfoot, S. Rae, I. Bond, V. Michaud, Progress in self-healing fiber-reinforced polymer composites, *Adv. Mater. Interfaces* 5 (2018) 1–20.
- [19] J. Ekeocha, C. Ellingford, M. Pan, A.M. Wemyss, C. Bowen, C. Wan, Challenges and opportunities of self-healing polymers and devices for extreme and hostile environments, *Adv. Mater.* 33 (2021) 1–37.
- [20] M.D. Hager, P. Greil, C. Leyens, S. van der Zwaag, U.S. Schubert, Self-healing materials, *Adv. Mater.* 22 (47) (2010) 5424–5430.
- [21] B. Blaiszik, S. Kramer, S. Olugebefola, J. Moore, N. Sottos, S. White, Self-healing polymers and composites, *Annu. Rev. Mater. Res.* 40 (2010) 179–211.
- [22] S.R. White, N.R. Sottos, P.H. Geubelle, J.S. Moore, M.R. Kessler, S.R. Sriram, E.N. Brown, S. Viswanathan, Autonomic healing of polymer composites, *Nature* 409 (6822) (2001) 794–797.
- [23] J.W. Pang, I.P. Bond, A hollow fibre reinforced polymer composite encompassing self-healing and enhanced damage visibility, *Compos. Sci. Technol.* 65 (11) (2005) 1791–1799.
- [24] K.S. Toohy, N.R. Sottos, J.A. Lewis, J.S. Moore, S.R. White, Self-healing materials with microvascular networks, *Nature Mater.* 6 (2007) 581–585.
- [25] J.F. Patrick, M.J. Robb, N.R. Sottos, J.S. Moore, S.R. White, Polymers with autonomous life-cycle control, *Nature* 540 (2016) 363–370.
- [26] A.R. Hamilton, N.R. Sottos, S.R. White, Self-healing of internal damage in synthetic vascular materials, *Adv. Mater.* 22 (2010) 5159–5163.
- [27] A.R. Hamilton, N.R. Sottos, S.R. White, Pressurized vascular systems for self-healing materials, *J. R. Soc. Interface* 70 (9) (2012) 1020–1028.
- [28] J.F. Patrick, K.R. Hart, B.P. Krull, C.E. Diesendruck, J.S. Moore, S.R. White, N.R. Sottos, Continuous self-healing life cycle in vascularized structural composites, *Adv. Mater.* 26 (2014) 4302–4308.
- [29] C.E. Diesendruck, N.R. Sottos, J.S. Moore, S.R. White, Biomimetic self-healing, *Angew. Chem. Int. Ed.* 54 (2015) 10428–10447.
- [30] K.R. Hart, S.M. Lankford, I.A. Freund, J.F. Patrick, B.P. Krull, E.D. Wetzel, N.R. Sottos, S.R. White, Repeated healing of delamination damage in vascular composites by pressurized delivery of reactive agents, *Compos. Sci. Technol.* 151 (2017) 1–9.
- [31] E.N. Brown, S.R. White, N.R. Sottos, Microcapsule induced toughening in a self-healing polymer composite, *J. Mater. Sci.* 39 (2004) 1703–1710.
- [32] A. Kousourakis, A.P. Mouritz, The effect of self-healing hollow fibres on the mechanical properties of polymer composites, *Smart Mater. Struct.* 19 (2010) 1–9.
- [33] S. Wang, M.W. Urban, Self-healing polymers, *Nat. Rev. Mater.* 5 (8) (2020) 562–583.
- [34] R. Ikura, J. Park, M. Osaki, H. Yamaguchi, A. Harada, Y. Takashima, Design of self-healing and self-restoring materials utilizing reversible and movable crosslinks, *NPG Asia Mater.* 14 (2022) 1–17.
- [35] K. Imato, M. Nishihara, T. Kanehara, Y. Amamoto, A. Takahara, H. Otsuka, Self-healing of chemical gels cross-linked by diarylbibenzofuranone-based trigger-free dynamic covalent bonds at room temperature, *Angew. Chem. Int. Ed.* 51 (2012) 1138–1142.
- [36] P. Cordier, F. Tournilhac, C. Soulié-Ziakovic, L. Leibler, Self-healing and thermoreversible rubber from supramolecular assembly, *Nature* 451 (7181) (2008) 977–980.
- [37] Z. Wei, J.H. Yang, J. Zhou, F. Xu, M. Zrínyi, P.H. Dussault, Y. Osada, Y.M. Chen, Self-healing gels based on constitutional dynamic chemistry and their potential applications, *Chem. Soc. Rev.* 43 (2014) 8114–8131.
- [38] D.L. Taylor, M. in het Panhuis, Self-healing hydrogels, *Adv. Mater.* 28 (2016) 9060–9093.
- [39] D. Montarnal, M. Capelot, F. Tournilhac, L. Leibler, Silica-like malleable materials for permanent organic networks, *Science* 334 (6058) (2011) 965–968.
- [40] X. Chen, M.A. Dam, K. Ono, A. Mal, H. Shen, S.R. Nutt, K. Sheran, F. Wudl, A thermally re-mendable cross-linked polymeric material, *Science* 295 (2002) 1698–1702.
- [41] J.S. Park, H.S. Kim, H. Thomas Hahn, Healing behavior of a matrix crack on a carbon fiber/mendomer composite, *Compos. Sci. Technol.* 69 (2009) 1082–1087.
- [42] C.-M. Chung, Y.-S. Roh, S.-Y. Cho, J.-G. Kim, Crack healing in polymeric materials via photochemical [2+2] cycloaddition, *Chem. Mater.* 16 (21) (2004) 3982–3984.
- [43] M.E. Garcia, Y. Lin, H.A. Sodano, Autonomous materials with controlled toughening and healing, *J. Appl. Phys.* 108 (9) (2010) 093512.
- [44] A.L.B. Ramirez, Z.S. Kean, J.A. Orlicki, M. Champhekar, S.M. Elsagr, W.E. Krause, S.L. Craig, Mechanochemical strengthening of a synthetic polymer in response to typically destructive shear forces, *Nature Chem.* 5 (2013) 757–761.
- [45] S. Hayes, F. Jones, K. Marshiya, W. Zhang, A self-healing thermosetting composite material, *Composites A* 38 (4) (2013) 1116–1120.
- [46] S. Meure, S. Furman, S. Khor, Poly[ethylene-co(methacrylic acid)] healing agents for mendable carbon fiber laminates, *Macromol. Mater. Eng.* 295 (2010) 420–424.

- [47] R.J. Varley, F. Charve, EMAA as a healing agent for mendable high temperature epoxy amine thermosets, *Composites A* 43 (2012) 1073–1080.
- [48] C.H. Wang, K. Sidhu, T. Yang, J. Zhang, R. Shanks, Interlayer self-healing and toughening of carbon fibre/epoxy composites using copolymer films, *Composites A* 43 (2012) 512–518.
- [49] K. Pingkarawat, T. Bhat, D.A. Craze, C.H. Wang, R.J. Varley, A.P. Mouritz, Healing of carbon fibre–epoxy composites using thermoplastic additives, *Polym. Chem.* 4 (2013) 5007–5015.
- [50] T. Yang, Y. Du, Z. Li, C. Wang, Mechanical properties of self-healing carbon fiber-epoxy composite stitched with mendable polymer fiber, *Polym. Polym. Compos.* 22 (2014) 329–336.
- [51] K. Pingkarawat, C. Dell’Olio, R. Varley, A. Mouritz, Poly(ethylene-co-methacrylic acid) (EMAA) as an efficient healing agent for high performance epoxy networks using diglycidyl ether of bisphenol a (DGEBA), *Polymer* 92 (2016) 153–163.
- [52] R.B. Ladani, K. Pingkarawat, A.T.T. Nguyen, C.H. Wang, A.P. Mouritz, Delamination toughening and healing performance of woven composites with hybrid z-fibre reinforcement, *Composites A* 110 (2018) 258–267.
- [53] A. Azevedo do Nascimento, F. Fernandez, F. S. da Silva, E. P.C. Ferreira, J.D. D. Melo, A.P. Cysne Barbosa, Addition of poly (ethylene-co-methacrylic acid) (EMAA) as self-healing agent to carbon-epoxy composites, *Composites A* 137 (2020) 106016.
- [54] T.W. Loh, R.B. Ladani, A. Orifici, E. Kandare, Ultra-tough and in-situ repairable carbon/epoxy composite with EMAA, *Composites A* 143 (2021) 1–10.
- [55] R.J. Varley, B. Dao, C. Pillsbury, S.J. Kalista, F.R. Jones, Low-molecular-weight thermoplastic modifiers as effective healing agents in mendable epoxy networks, *J. Intell. Mater. Syst. Struct.* 25 (1) (2014) 107–117.
- [56] S. Meure, D.-Y. Wu, S.A. Furman, FTIR study of bonding between a thermoplastic healing agent and a mendable epoxy resin, *Vib. Spectrosc.* 52 (2010) 10–15.
- [57] S. Meure, R.J. Varley, D.Y. Wu, S. Mayo, K. Nairn, S. Furman, Confirmation of the healing mechanism in a mendable EMAA–epoxy resin, *Eur. Polym. J.* 48 (2012) 524–531.
- [58] A.D. Snyder, Z.J. Phillips, J.S. Turicek, C.E. Diesendruck, K.B. Nakshatrala, J.F. Patrick, Prolonged in situ self-healing in structural composites via thermo-reversible entanglement, *Nature Commun.* 13 (2022) 1–12.
- [59] S. Hashemi, A.J. Kinloch, J.G. Williams, Corrections needed in double-cantilever beam tests for assessing the interlaminar failure of fibre-composites, *J. Mater. Sci. Lett.* 8 (1989) 125–129.
- [60] B. Krull, J. Patrick, K. Hart, S. White, N. Sottos, Automatic optical crack tracking for double cantilever beam specimens, *Exp. Tech.* 40 (2015) 937–945.
- [61] A.J. Kinloch, J.G. Williams, Crack blunting mechanisms in polymers, *J. Mater. Sci.* 15 (4) (1980) 987–996.
- [62] N. Alif, L.A. Carlsson, L. Boogh, The effect of weave pattern and crack propagation direction on mode I delamination resistance of woven glass and carbon composites, *Composites B* 29 (1998) 603–611.